

Squeezing information from radio surveys to probe the primordial Universe

Dionysios Karagiannis^{1,11}, Roy Maartens^{1,2,3}, Shun Saito^{4,5},
 José Fonseca^{6,7,1}, Stefano Camera^{8,9,10,1}, Chris Clarkson^{11,1,12}

¹*Department of Physics & Astronomy, University of the Western Cape, Cape Town 7535, South Africa*

²*Institute of Cosmology & Gravitation, University of Portsmouth, Portsmouth PO1 3FX, United Kingdom*

³*National Institute for Theoretical & Computational Sciences, Cape Town 7535, South Africa*

⁴*Institute for Multi-messenger Astrophysics & Cosmology, Department of Physics,
 Missouri University of Science & Technology, Rolla MO65409, USA*

⁵*Kavli Institute for the Physics & Mathematics of the Universe,
 University of Tokyo, Kashiwa, Chiba 227-8583, Japan*

⁶*Instituto de Astrofísica e Ciências do Espaço, Universidade do Porto CAUP, 4150-762 Porto, Portugal*

⁷*Departamento de Física e Astronomia, Faculdade de Ciências,
 Universidade do Porto, Rua do Campo Alegre 687, PT4169-007 Porto, Portugal*

⁸*Dipartimento di Fisica, Università degli Studi di Torino, 10125 Torino, Italy*

⁹*INFN – Istituto Nazionale di Fisica Nucleare, Sezione di Torino, 10125 Torino, Italy*

¹⁰*INAF – Istituto Nazionale di Astrofisica, Osservatorio Astrofisico di Torino, 10025 Pino Torinese, Italy*

¹¹*Department of Physics & Astronomy, Queen Mary University of London, London E1 4NS, United Kingdom*

¹²*Department of Mathematics & Applied Mathematics,
 University of Cape Town, Cape Town 7701, South Africa*

A major goal of cosmology is to understand the nature of the field(s) which drove primordial Inflation. Through future observations, the statistics of large-scale structure will allow us to probe primordial non-Gaussianity of the curvature perturbation at the end of Inflation. We show how a new correlation statistic can significantly improve these constraints over conventional methods. Next-generation radio telescope arrays are under construction which will map the density field of neutral hydrogen to high redshifts. These telescopes can operate as an interferometer, able to probe small scales, or as a collection of single dishes, combining signals to map the large scales. We show how to fuse these these operating modes in order to measure the squeezed bispectrum with higher precision and greater economy. This leads to constraints on primordial non-Gaussianity that will improve on measurements by Planck, and out-perform other surveys such as Euclid. We forecast that $\sigma(f_{\text{NL}}^{\text{loc}}) \sim 3$, achieved by using a small subset, $\mathcal{O}(10^2 - 10^3)$, of the total number of accessible triangles. The proposed method can be used for any signal that peaks in squeezed configurations.

INTRODUCTION

Primordial non-Gaussianity (PNG) is one of the most promising observational avenues to probe the primordial Universe, due to its sensitivity to the physics of these early stages. Measuring PNG could reveal the field content and the amplitude of field interactions [1], as well as verify the quantum nature of the primordial fluctuations [2] that seed the large-scale structure (LSS) we observe today, as predicted by Inflation. This early Universe information can be extracted by characterizing how much the distribution of the primordial perturbations deviates from Gaussianity.

We propose a novel method that utilises the functionalities of a radio telescope array in 21cm intensity mapping surveys, in order to measure the bispectrum of squeezed triangles, in an optimal and efficient way, while maximizing the PNG signal and avoiding regions contaminated by systematics. The squeezed bispectrum, with $k_1 \approx k_2 \gg k_3$, can be used to significantly improve current bounds on local PNG [3–6]. Constraining $f_{\text{NL}}^{\text{loc}}$ provides a unique observational handle to rule out entire classes of inflationary models and enhance our knowledge

of the early Universe [7].

Currently, the tightest constraints on PNG are from cosmic microwave background (CMB) measurements [8]. The results imply that the primordial perturbation field is weakly non-Gaussian and hence most of the PNG information is contained in the primordial bispectrum, i.e. the lowest-order deviation from a Gaussian distribution. Most of the available information on local PNG from the CMB anisotropies bispectrum has been extracted. LSS surveys have the potential to significantly improve the current PNG bounds [9, 10], since a 3D dark matter tracer (e.g. galaxies) has considerably more bispectrum modes than the 2D CMB. However, most of these LSS modes are in the nonlinear regime, which is dominated by the gravitational evolution of cosmic structures. The subdominant PNG signal must be separated from the late-time non-Gaussian gravitational contributions with significant precision. Recent results from optical galaxy surveys [11–15], where an analytical perturbative model has been used (see e.g. [16]), are far from being competitive with the CMB bounds. The main reason is the complexity of accurate analytical models beyond the perturbative regime which is needed to extract the wealth of

PNG information from the nonlinear scales. A promising alternative is to rely on numerical approaches, like simulation-based [17–20] or field-level inference [21, 22].

In this letter, we employ a perturbative analysis at high redshifts, which facilitates access to a large number of bispectrum modes in the perturbative regime. By also using high-density samples, we can significantly boost the PNG signal. To achieve this, we investigate upcoming high-redshift 21cm intensity mapping surveys [23–30], focusing on the squeezed bispectrum, $k_1 \approx k_2 \gg k_3$. Due to its distinct triangle preference, which couples different scales, this shape is mostly orthogonal to the late-time gravitational part of the LSS bispectrum and therefore relatively easier to separate from the latter.

PNG FROM 21CM INTENSITY MAPPING

In the post-reionization Universe most of the neutral hydrogen (HI) resides inside galaxies, thus detecting its 21cm emission line provides a tracer of the underlying matter distribution. The HI intensity mapping (IM) technique consists of making brightness temperature maps of the sky at different radio frequencies, by measuring the integrated emission line from many galaxies that reside within each pixel. The combined emission yields a large detectable signal, while probing very large volumes of the Universe from the epoch of reionisation up to present times. Such spectroscopic surveys are planned for example with the Square Kilometre Array Observatory (SKAO) [29] and the Hydrogen Intensity and Real-time Analysis eXperiment (HIRAX) [30] and will cover a wide sky area and deep redshift range ($0 < z \lesssim 3$).

An array of radio telescopes are set up to measure HI intensity in two distinct ways: in single-dish (SD) mode, by auto-correlating the signal of each dish individually or in interferometer mode (IF), where the signal from all dishes is cross-correlated. The first probes the large and linear scales of clustering, while the latter probes the intermediate to the very small and nonlinear scales (large k -mode values) with high angular resolution. Both modes of the instrument compliment each other in Fourier space, as shown in the schematic illustration of Fig. 1. Additionally the two functionalities differ in the behaviour of the instrumental noise, which is the dominant noise contribution [31]. Contrary to optical surveys, the shot noise can be negligible, up to small scales.

In addition to the intrinsic instrumental scale limitations of an HI IM survey, there are additional known systematics. Astrophysical sources introduce smooth foregrounds which overwhelm the very large-scale fluctuations along the line of sight ($k_{\parallel} \lesssim 0.01 h/\text{Mpc}$) rendering them unusable [32–38]. In the case of an interferometer, a further non-smooth foreground component, called the foreground wedge, contaminates some of the modes

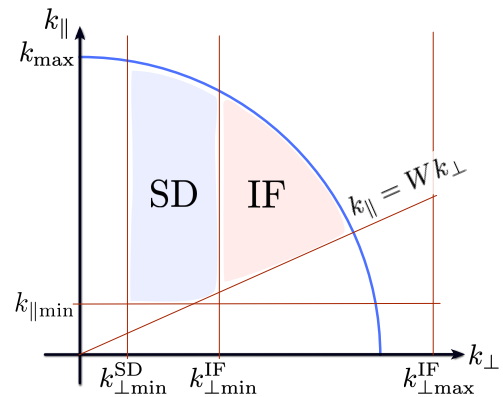


FIG. 1: Schematic illustration of the ranges of radial and transverse wavenumbers that the two survey modes are sensitive to (adapted from [43]).

transverse to the line of sight [35, 36, 39–42]. In Fig. 1 we present a schematic illustration showing the observation window, in Fourier space, for each observing mode of the HI IM instrument.

The presence of local PNG induces a large-scale scale-dependent behaviour on the power spectrum of a tracer [44–49]. Hence, a LSS survey should be able to probe the largest scales of clustering in order to provide competitive constraints on $f_{\text{NL}}^{\text{loc}}$. Moreover, attaining a deeper comprehension of galaxy formation is essential for establishing constraints on the amplitude of local PNG [50–52]. For the bispectrum, access to a wide scale range is essential, in order to probe enough squeezed triangles and boost the signal-to-noise ratio. Thus, a single-dish HI IM survey favours a power spectrum analysis, where has been suggested as well in the past as a powerful probe for local PNG [53–57], outperforming an interferometer survey. The reverse holds for the bispectrum $f_{\text{NL}}^{\text{loc}}$ constraints, where surveys designed for IF mode outshine those in SD mode [58].

Due to the intrinsic instrumental and observational scale restrictions, HI IM surveys have not yet reached their full potential in constraining $f_{\text{NL}}^{\text{loc}}$, despite their optimal specifications (i.e. wide sky area, high redshifts and sample densities). This is even more evident for the bispectrum of an IF survey, where a more futuristic setup, like PUMA [59] or SKA2 LOW [60] is required to significantly improve over current bounds [58, 61].

THE 21CM BIMODAL BISPECTRUM

In this Letter, we propose a novel method to push the capabilities of HI IM to tightly constrain the amplitude of local PNG, while excluding the contaminated k -modes from the analysis. The key observation lies in the fact that the two functionalities of the radio telescope probe complimentary scales (see Fig. 1). Combining the data

from these two can provide access to a very wide scale range with high resolution: from the large and linear scales, as probed by SD mode, up to the very small and nonlinear ones, measured by IF mode. This is optimal for a bispectrum analysis and especially for an observable that has a strong signal on squeezed triangles, like local PNG.

Squeezed configurations correlate different scales, i.e. one side of the triangle is much smaller than the other two ($k_1 \sim k_2 \gg k_3$). Thus, cross correlating a density field $\delta^{\text{SD}}(\mathbf{k})$, as probed by a single-dish mode survey, with two density fields $\delta^{\text{IF}}(\mathbf{k})$ probed by a survey in interferometer mode, we can form an HI IM bispectrum that has access to a very large number of squeezed triangles. We define the bimodal bispectrum, synergising two HI IM surveys in two different operating modes, for an overlapping redshift range and sky area, as

$$\langle \delta^{\text{IF}}(\mathbf{k}_1) \delta^{\text{IF}}(\mathbf{k}_2) \delta^{\text{SD}}(\mathbf{k}_3) \rangle = (2\pi)^3 \delta_{\text{D}}(\mathbf{k}_{123}) B^{\text{SD} \times \text{IF}}(\mathbf{k}_1, \mathbf{k}_2, \mathbf{k}_3), \quad (1)$$

where $\mathbf{k}_{123} \equiv \mathbf{k}_1 + \mathbf{k}_2 + \mathbf{k}_3$ and the Dirac δ_{D} ensures momentum conservation.

The fields $\delta^{\text{SD,IF}}$ are fluctuations in the 21cm brightness temperature and their measurements in Fourier space depend on survey window functions $W^{\text{SD,IF}}(\mathbf{k})$. Crucially, SD observations observe the actual sky, so that the fluctuation is a convolution in Fourier space, $\delta^{\text{SD}}(\mathbf{k}) = W^{\text{SD}}(\mathbf{k}) \star \delta(\mathbf{k})$, whereas IF mode measures a Fourier transform of the sky, leading to a simple product, $\delta^{\text{IF}}(\mathbf{k}) = W^{\text{IF}}(\mathbf{k}) \delta(\mathbf{k})$. Here and below we omit the z -dependence for brevity.

The window function $W^{\text{SD,IF}}(\mathbf{k})$ incorporates the observational window of each instrumental mode. It ensures that the measured k -modes are well within the intrinsic instrumental limits and away from regions affected by systematics (see Fig. 1), giving a contamination-free measurement of the synergy bispectrum. These limits include the fundamental limitations of each instrument [43], which among others depend on the size of the dishes of each survey, as well as the known astrophysical foregrounds and the wedge effect in the case of the IF mode. The latter two exclude all scales that satisfy $k_{\parallel} < k_{\parallel \text{min}}$ and $k_{\parallel} < k_{\text{wedge}}(z) k_{\perp}$ [58]. In the case of the foregrounds it has been proposed that they can be recovered with percent precision [62–66], thus we consider an optimistic cut-off value, $k_{\parallel \text{min}} = 0.005 h/\text{Mpc}$.

The estimator for measuring the synergy bispectrum between the SD and IF modes of the neutral hydrogen instrument is

$$\hat{B}^{\text{SD} \times \text{IF}}(\mathbf{k}_1, \mathbf{k}_2, \mathbf{k}_3) = \frac{1}{V_s V_{123}} \sum_{\mathbf{q}_1 \in k_1} \sum_{\mathbf{q}_2 \in k_2} \sum_{\mathbf{q}_3 \in k_3} \delta_{\text{K}}(\mathbf{q}_{123}) \times \delta^{\text{IF}}(\mathbf{q}_1) \delta^{\text{IF}}(\mathbf{q}_2) \delta^{\text{SD}}(\mathbf{q}_3), \quad (2)$$

where V_s is the volume of the survey within each redshift bin. The Kronecker delta ensures the formation of

‘fundamental triangles’ with sides \mathbf{q}_i , satisfying $\mathbf{q}_{123} = 0$, that fall in the ‘triangular bin’ of width Δk defined by the bin centres (k_1, k_2, k_3) . The volume in Fourier space of the fundamental triangle bins is, in the thin shell limit $V_{123} = 8\pi^2 k_1 k_2 k_3 \Delta k^3$ [67], where the bin size Δk is taken to be the fundamental frequency of the survey, $\Delta k = k_{\text{f}} = 2\pi/V_s^{1/3}$. For the extreme cases of flattened ($k_1 = k_2 + k_3$) and open triangles ($k_1 \neq k_2 + k_3$) this expression breaks. Here we consider the analytic corrections for these configurations presented in [68].

The covariance of the bimodal bispectrum estimator is given by

$$\mathbf{C}_{ij} \equiv \langle \delta \hat{B}_i \delta \hat{B}_j \rangle = \mathbf{C}_{ij}^{\text{G}} + \mathbf{C}_{ij}^{\text{NG}}, \quad (3)$$

where $\delta \hat{B}_i = \hat{B}_i - \langle \hat{B}_i \rangle$, i and j indices denote the different triangle configuration, i.e. $B_i \equiv B(k_1^i, k_2^i, k_3^i)$, and G, NG are the Gaussian and non-Gaussian contributions. In the thin shell limit ($k \gg \Delta k$), the Gaussian part can be written as

$$\mathbf{C}_{ij}^{\text{G}} = \frac{(2\pi)^6}{V_s V_{123}} s_{123} \delta_{ij} P_{\text{HI}}^{\text{IF}}(\mathbf{k}_1) P_{\text{HI}}^{\text{IF}}(\mathbf{k}_2) P_{\text{HI}}^{\text{SD}}(\mathbf{k}_3), \quad (4)$$

where $s_{123} = 6, 2, 1$ for equilateral, isosceles and scalene triangles respectively. The HI IM power spectrum is the tree-level model, including the instrumental noise and shot noise [58] (see also the Appendix).

The non-Gaussian part of the covariance is a complicated quantity to calculate analytically. However, in the case of squeezed configurations, like those considered in this work, it can be accurately approximated by [68–70]

$$\mathbf{C}_{ij}^{\text{NG}} = \frac{2(2\pi)^3}{V_s V_{123}^i V_{123}^j} \left[\delta_{k_1^i k_1^j} U(k_1^i, k_1^j) \times B_{\text{HI}}(\mathbf{k}_1^j, \mathbf{k}_2^i, \mathbf{k}_3^i) B_{\text{HI}}(\mathbf{k}_1^i, \mathbf{k}_2^j, \mathbf{k}_3^j) + 8 \text{perm} \right], \quad (5)$$

where $U(k_1^i, k_1^j) = 16\pi^3 k_2^i k_3^i k_2^j k_3^j \Delta k^5$. For the extreme triangle configurations, we consider the analytic corrections presented in Ref. [68]. For the HI IM bispectrum, B_{HI} , the tree-level model is considered [58] (see also the Appendix). A well motivated assumption for the instrumental noise is that it is Gaussian [43]; in this case the non-Gaussian part of the covariance will not contain instrumental noise contributions.

RESULTS

In this section, we present forecasts for the HI IM bimodal bispectrum on constraining the amplitude of local PNG. The Fisher information matrix formalism is used, which provides the minimum error on a parameter achieved by a survey setup, while requiring only an analytic model as an input. In a given redshift bin the

Fisher matrix is

$$F_{\alpha\beta} = \int d^3\mathbf{k}_i \frac{\partial B^{\text{SD}\times\text{IF}}(\mathbf{k}_i)}{\partial\theta_\alpha} C_{ij}^{-1} \frac{\partial B^{\text{SD}\times\text{IF}}(\mathbf{k}_j)}{\partial\theta_\beta}. \quad (6)$$

Here θ_α are the parameters of interest (see the Appendix for the parameter vector), \mathbf{k}_i is an abbreviation for the three sides of the i th triangle, and $\int d^3\mathbf{k}_i \equiv 1/(4\pi) \int_{-1}^1 d\mu_1 \int_0^{2\pi} d\phi \sum_T$, where $\mu_1 = \hat{\mathbf{k}}_1 \cdot \hat{\mathbf{z}}$ and ϕ characterize polar and the azimuthal orientations of a triangle relative to the line-of-sight direction, $\hat{\mathbf{z}}$ (see [71] for a discussion and alternative parameterisations). The forecasts presented here come from the angle-averaged bispectrum. The sum \sum_T is over all the Fourier space triangles that satisfy $k_{\min} \leq k_3 \leq k_2 \leq k_1 \leq k_{\max}$.

Here we only consider a squeezed subset of these configurations, i.e. those that satisfy $k_1 \approx k_2 \geq 3k_3$, since they contain most of the signal for the local PNG. Note, that the bimodal bispectrum can benefit all triangle shapes (see the Appendix). The minimum value is $k_{\min} = k_{\text{f}}$, which is the largest scale probed in the redshift bin by the survey, and the maximum value k_{\max} corresponds to the smallest scale where the theoretical model is reliable. We use a conservative choice $k_{\max}(z) = 0.75 k_{\text{NL}}(z)$ and an optimistic one $k_{\max}(z) = k_{\text{NL}}(z)$, where k_{NL} is given by the inverse square root of the one-dimensional velocity dispersion [61]. The analysis is thus confined within the perturbative regime, where the tree-level model offers good agreement with the numerical results [72–76]. The tree-level description is used to model the expected value of the bimodal estimator [Eq. (2)], including the observational windows for the two operating modes of the instrument. Any \mathbf{k} -mode outside of the window will result in the exclusion of the triangle from the Fisher matrix calculation.

The forecast error on θ_α is then given by $\sigma(\theta_\alpha) = (\tilde{F}_{\alpha\alpha}^{-1})^{1/2}$, where $\tilde{F}_{\alpha\beta} = \Sigma_i F_{\alpha\beta}(z_i)$ encompasses the total information from all redshift bins considered. All the parameters that control the model are considered free and are entries of the Fisher matrix. These include the Λ CDM cosmology parameters and the HI IM bias parameters [9, 58, 61, 78] (see the Appendix, and [79] for further details on the Fisher formalism).

All work on constraining $f_{\text{NL}}^{\text{loc}}$ is affected by a degeneracy between $f_{\text{NL}}^{\text{loc}}$ and b_ϕ (see e.g. [51, 80]), where b_ϕ is the local PNG bias parameter [48, 81]. This compromises the ability of the LSS power spectrum and bispectrum to tightly constrain $f_{\text{NL}}^{\text{loc}}$. PNG bias depends on the halo formation history [82], i.e., on properties beyond total mass. If it is accurately modeled and constrained, e.g. with hydrodynamical simulations, this degeneracy is broken and the power of the LSS bispectrum to constrain $f_{\text{NL}}^{\text{loc}}$ is completely restored [52]. Our focus here is on the relative improvement from a new bimodal synergy, compared to the sum of the standard bispectrum information from 2 surveys – therefore, our results are not affected by the

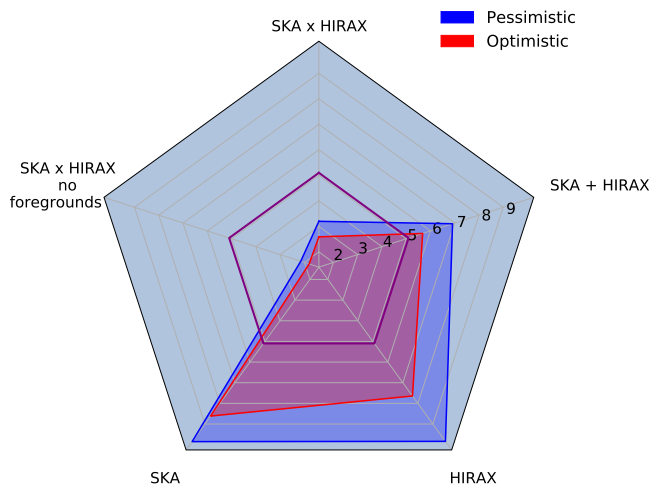


FIG. 2: Marginalized forecasts of $\sigma(f_{\text{NL}}^{\text{loc}})$ from the bimodal bispectrum (SKA \times HIRAX) with and without foreground cut, for pessimistic and optimistic k_{\max} . Forecasts from each survey and from the summed signal without cross correlation (SKA + HIRAX) are also shown. Purple line is the Planck 2018 constraint [77].

model for b_ϕ , and we use the simplest model that breaks the degeneracy [44–46].

After marginalization over the free parameters of the model [58, 78] (see also the Appendix), we retrieve the final forecasts on $f_{\text{NL}}^{\text{loc}}$ from the bimodal bispectrum. The two surveys that we consider are Band 1 of SKA-MID [29], which is a radio telescope in SD mode and has a redshift range of $z = 0.35 - 3.05$, and the final version of HIRAX [30] in IF mode with $z = 0.75 - 2.55$. In the analysis, we consider only the signal from the overlapping range ($z = 0.75 - 2.55$) and sky coverage ($15,000 \text{ deg}^2$). For details of the surveys considered and the specifics of the instrumental noise, see [78]. Note that the same survey can be used, operating in SD and IF mode, to produce the bimodal synergy. However, telescope design is usually optimized for one of the modes and is not effective in the other.

The forecasts on $f_{\text{NL}}^{\text{loc}}$ from the synergy between SKA and HIRAX are presented in Fig. 2, for the pessimistic and optimistic k_{\max} cases. The results when removing the foreground cut, i.e. when assuming perfect foreground cleaning and signal reconstruction, are shown in order to illustrate the limiting capabilities of the surveys. We also present the forecasts from each individual survey, as well as their summed signal (SKA+HIRAX) without cross-correlation, for the same redshift range and squeezed configurations as in the bimodal case. This allows for a fair comparison and an assessment of the gain from the proposed method. The results indicate that the bimodal bispectrum provides a significant improvement on $f_{\text{NL}}^{\text{loc}}$ constraints, more than a factor of 3, compared

to those from each individual survey, as well as their summed signal (a factor of ~ 3).

The constraints are competitive with current CMB bounds, exhibiting a factor of ~ 2 improvement. The bimodal bispectrum achieves this by only using a small subset, $\mathcal{O}(10^2 - 10^3)$ triangles, of the total number of formed triangles. This means that the forecasts could improve further once all the triangles are considered, even achieving $\sigma(f_{\text{NL}}^{\text{loc}}) \lesssim 1$, as in the case of dedicated surveys (e.g. SPHEREx [83] or PUMA [84]). In addition, by including the single-survey information from the non-overlapping redshifts and sky area, the constraints would improve even further and utilise to the fullest the available signal in the SKA-HIRAX synergy.

CONCLUSIONS

The MeerKLASS pilot survey [85] on the MeerKAT precursor telescope of SKA-MID, has provided HI IM maps both in SD and IF mode. This has allowed the detection of the SD power spectrum in cross correlation with galaxies [86] and the auto-power in IF mode [87]. The measurements in SD mode will see a major advance when the SKA is operating, while the early IF mode measurements will be vastly improved when HIRAX takes data.

We have shown how to combine these observations in a novel way to give significantly stronger constraints on $f_{\text{NL}}^{\text{loc}}$ than was previously thought possible. In fact, this method will improve on the Planck results by around a factor of 2, using only a few thousand triangles per redshift bin. The bimodal bispectrum improves constraints relative to the sum of the individual surveys by a factor of ~ 4 , which is equivalent to a much larger SD or IF array. It is in fact the only way to get any strong constraints on local PNG from the HI intensity bispectrum.

We highlight the point that a substantial part of the constraining power comes from the IF mode signal. Therefore, the results will improve even further if the IF instrumental noise can be reduced. By contrast, the method is not so sensitive to the SD mode noise (see Fig. 4). Instead, the SD signal is sensitive to the loss of very large scales $k_{\parallel} < k_{\parallel\text{min}}$ (see Figs. 3 and 5), so that further improvement requires advances in foreground cleaning and long-wavelength k_{\parallel} -mode reconstruction.

Long-wavelength modes provide a set of very squeezed triangles that carry a significant amount of signal on local PNG. On the other hand, increasing the number of squeezed triangles by changing k_{max} (i.e. the pessimistic and optimistic cases) provides a much less pronounced gain in the $f_{\text{NL}}^{\text{loc}}$ constraints ($\sim 20\%$). Notably, the constraints with an optimistic k_{max} are very close ($\sim 15\%$ difference) to those provided by the pessimistic case, in which no radial foregrounds are considered (see Fig. 2).

This indicates that the local PNG signal lost to foregrounds can be partially recovered, by venturing further into the intermediate regime. Smaller scales have a significant amount of information on PNG, which requires alternative methods to the analytical modelling, e.g. simulated-based inference [17–20]. We leave this for future work.

The bimodal bispectrum cross-correlates SD large scales with smaller-scale IF modes. We do not expect foregrounds or instrumental systematics to show correlations between long- and short-wavelength k -modes. This is another advantage of the bimodal synergy. The advantages of the bimodal bispectrum are not limited to local PNG studies. Any observable that has signal peaking on the squeezed triangles can benefit from the proposed synergy. Moreover, including all shapes of triangles into the bimodal analysis (see Fig. 6), still maintains a significant gain in the constraining power.

In the case of bispectrum probes of optical surveys, the data are observed in real space, thus a Fourier transformation takes place from the observed three-point correlation function, including the window functions for each side of the triangle. This introduces complex convolutions between the windows and significantly hinders a bispectrum analysis. In the case of the bimodal synergy bispectrum, the IF mode measures a Fourier transformation of the sky, while the SD mode the actual sky, including the observational windows. This means that the window convolutions will be much more under control, offering an additional benefit to the proposed approach.

Acknowledgements DK, RM and SS acknowledge support for this work from the University of Missouri South African Education Program. RM is supported by the South African Radio Observatory and National Research Foundation (grant no. 75415). SS acknowledges support for this work from NSF-2219212. SS is supported in part by World Premier International Research Center Initiative, MEXT, Japan. SC acknowledges support from the Italian Ministry of University and Research, PRIN 2022 ‘EXSKALIBUR – Euclid-Cross-SKA: Likelihood Inference Building for Universe Research’, from the Italian Ministry of Foreign Affairs and International Cooperation (grant no. ZA23GR03), and from the European Union – Next Generation EU. JF acknowledges support of Fundação para a Ciência e a Tecnologia through the Investigador FCT Contract No. 2020.02633.CEECIND/CP1631/CT0002, the FCT project PTDC/FIS-AST/0054/2021, and the research grants UIDB/04434/2020 and UIDP/04434/2020.

[1] R. de Putter, J. Gleyzes, and O. Doré, Phys. Rev. D **95**, 123507 (2017), arXiv:1612.05248 [astro-ph.CO].

- [2] D. Green and R. A. Porto, *Phys. Rev. Lett.* **124**, 251302 (2020), arXiv:2001.09149 [hep-th].
- [3] D. S. Salopek and J. R. Bond, *Phys. Rev. D* **42**, 3936 (1990).
- [4] A. Gangui, F. Lucchin, S. Matarrese, and S. Mollerach, *ApJ* **430**, 447 (1994), astro-ph/9312033.
- [5] L. Verde, L. Wang, A. F. Heavens, and M. Kamionkowski, *MNRAS* **313**, 141 (2000), astro-ph/9906301.
- [6] E. Komatsu and D. N. Spergel, *Phys. Rev. D* **63**, 063002 (2001), astro-ph/0005036.
- [7] A. Achúcarro, M. Biagetti, M. Braglia, G. Cabass, E. Castorina, R. Caldwell, X. Chen, W. Coulton, R. Flauger, J. Fumagalli, M. M. Ivanov, H. Lee, A. Maleknejad, P. D. Meerburg, A. Moradinezhad Dizgah, G. A. Palma, S. Renaux-Petel, G. L. Pimentel, B. Wallisch, B. D. Wandelt, L. T. Witkowski, and W. L. Kimmy Wu, arXiv e-prints, arXiv:2203.08128 (2022), arXiv:2203.08128 [astro-ph.CO].
- [8] Y. Akrami *et al.* (Planck), *Astron. Astrophys.* **641**, A9 (2020), arXiv:1905.05697 [astro-ph.CO].
- [9] D. Karagiannis, A. Lazanu, M. Liguori, A. Raccanelli, N. Bartolo, and L. Verde, *MNRAS* **478**, 1341 (2018), arXiv:1801.09280 [astro-ph.CO].
- [10] P. D. Meerburg, D. Green, R. Flauger, B. Wallisch, M. C. D. Marsh, E. Pajer, G. Goon, C. Dvorkin, A. M. Dizgah, D. Baumann, G. L. Pimentel, S. Foreman, E. Silverstein, E. Chisari, B. Wandelt, M. Loverde, and A. Slosar, *Bull. Am. Astron. Soc.* **51**, 107 (2019), arXiv:1903.04409 [astro-ph.CO].
- [11] E. Castorina, N. Hand, U. Seljak, F. Beutler, C.-H. Chuang, C. Zhao, H. Gil-Marín, W. J. Percival, A. J. Ross, P. D. Choi, K. Dawson, A. de la Macorra, G. Rossi, R. Ruggeri, D. Schneider, and G.-B. Zhao, *Journal of Cosmology and Astro-Particle Physics* **2019**, 010 (2019), arXiv:1904.08859 [astro-ph.CO].
- [12] E.-M. Mueller, M. Rezaie, W. J. Percival, A. J. Ross, R. Ruggeri, H.-J. Seo, H. Gil-Marín, J. Bautista, J. R. Brownstein, K. Dawson, A. de la Macorra, N. Palanque-DeLabrouille, G. Rossi, D. P. Schneider, and C. Yeche (eBOSS), *Mon. Not. Roy. Astron. Soc.* **514**, 3396 (2022), arXiv:2106.13725 [astro-ph.CO].
- [13] G. Cabass, M. M. Ivanov, O. H. E. Philcox, M. Simonović, and M. Zaldarriaga, *Phys. Rev. Lett.* **129**, 021301 (2022), arXiv:2201.07238 [astro-ph.CO].
- [14] G. D'Amico, M. Lewandowski, L. Senatore, and P. Zhang, (2022), arXiv:2201.11518 [astro-ph.CO].
- [15] G. Cabass, M. M. Ivanov, O. H. E. Philcox, M. Simonović, and M. Zaldarriaga, *Phys. Rev. D* **106**, 043506 (2022), arXiv:2204.01781 [astro-ph.CO].
- [16] M. M. Ivanov, O. H. E. Philcox, T. Nishimichi, M. Simonović, M. Takada, and M. Zaldarriaga, *Phys. Rev. D* **105**, 063512 (2022), arXiv:2110.10161 [astro-ph.CO].
- [17] G. Jung, D. Karagiannis, M. Liguori, M. Baldi, W. R. Coulton, D. Jamieson, L. Verde, F. Villaescusa-Navarro, and B. D. Wandelt, *Astrophys. J.* **940**, 71 (2022), arXiv:2206.01624 [astro-ph.CO].
- [18] W. R. Coulton, F. Villaescusa-Navarro, D. Jamieson, M. Baldi, G. Jung, D. Karagiannis, M. Liguori, L. Verde, and B. D. Wandelt, *Astrophys. J.* **943**, 64 (2023), arXiv:2206.01619 [astro-ph.CO].
- [19] G. Jung, D. Karagiannis, M. Liguori, M. Baldi, W. R. Coulton, D. Jamieson, L. Verde, F. Villaescusa-Navarro, and B. D. Wandelt, *Astrophys. J.* **948**, 135 (2023), arXiv:2211.07565 [astro-ph.CO].
- [20] W. R. Coulton, F. Villaescusa-Navarro, D. Jamieson, M. Baldi, G. Jung, D. Karagiannis, M. Liguori, L. Verde, and B. D. Wandelt, *Astrophys. J.* **943**, 178 (2023), arXiv:2206.15450 [astro-ph.CO].
- [21] D. Baumann and D. Green, *JCAP* **08**, 061 (2022), arXiv:2112.14645 [astro-ph.CO].
- [22] A. Andrews, J. Jasche, G. Lavaux, and F. Schmidt, *Mon. Not. Roy. Astron. Soc.* **520**, 5746 (2023), arXiv:2203.08838 [astro-ph.CO].
- [23] S. Bharadwaj, B. Nath, B. B. Nath, and S. K. Sethi, *J. Astrophys. Astron.* **22**, 21 (2001), arXiv:astro-ph/0003200.
- [24] R. A. Battye, R. D. Davies, and J. Weller, *Mon. Not. Roy. Astron. Soc.* **355**, 1339 (2004), arXiv:astro-ph/0401340.
- [25] S. Wyithe and A. Loeb, *Mon. Not. Roy. Astron. Soc.* **383**, 606 (2008), arXiv:0708.3392 [astro-ph].
- [26] T.-C. Chang, U.-L. Pen, J. B. Peterson, and P. McDonald, *Phys. Rev. Lett.* **100**, 091303 (2008), arXiv:0709.3672 [astro-ph].
- [27] R. A. Battye, I. W. A. Browne, C. Dickinson, G. Heron, B. Maffei, and A. Pourtsidou, *MNRAS* **434**, 1239 (2013), arXiv:1209.0343 [astro-ph.CO].
- [28] M. G. Santos *et al.*, *PoS AASKA14*, 019 (2015), arXiv:1501.03989 [astro-ph.CO].
- [29] D. J. Bacon *et al.* (SKA), *Publ. Astron. Soc. Austral.* **37**, e007 (2020), arXiv:1811.02743 [astro-ph.CO].
- [30] D. Crichton, M. Aich, A. Amara, K. Bandura, B. A. Bassett, C. Bengaly, P. Berner, S. Bhatporia, M. Bucher, T.-C. Chang, H. C. Chiang, J.-F. Cliche, C. Crichton, R. Dave, D. I. L. De Villiers, M. Dobbs, A. M. Ewall-Wice, S. Eyono, C. Finlay, S. Gaddam, K. Ganga, K. G. Gayley, K. Gerodias, T. B. Gibbon, A. Gumba, N. Gupta, M. Harris, H. Heilgendorff, M. Hilton, A. D. Hincks, P. Hitz, M. Jalilvand, R. P. M. Julie, Z. Kader, J. Kania, D. Karagiannis, A. Karastergiou, K. Kesebonye, P. Kittiwisit, J.-P. Kneib, K. Knowles, E. R. Kuhn, M. Kunz, R. Maartens, V. MacKay, S. MacPherson, C. Monstein, K. Moodley, V. Mugundhan, W. Naidoo, A. Naidu, L. B. Newburgh, V. Nistane, A. Di Nitto, D. Ölçek, X. Pan, S. Paul, J. B. Peterson, E. Pieters, C. Pieterse, A. Pillay, A. R. Polish, L. Randrianjanahary, A. Refregier, A. Renard, E. Retana-Montenegro, I. H. Rout, C. Russeawon, A. V. Sadr, B. R. B. Saliwanchik, A. Sampath, P. Sanghavi, M. G. Santos, O. Sengate, J. R. Shaw, J. L. Sievers, O. M. Smirnov, K. M. Smith, U. A. M. Sob, R. Srianand, P. Stronkhorst, D. D. Sunder, S. Tartakovsky, R. Taylor, P. Timbie, E. E. Tolley, J. Townsend, W. Tyndall, C. Ungerer, J. van Dyk, G. van Vuuren, K. Vanderlinde, T. Viant, A. Walters, J. Wang, A. Weltman, P. Woudt, D. Wulf, A. Zavyalov, and Z. Zhang, *Journal of Astronomical Telescopes, Instruments, and Systems* **8**, 011019 (2022), arXiv:2109.13755 [astro-ph.IM].
- [31] Y. Gong, X. Chen, M. Silva, A. Cooray, and M. G. Santos, *ApJ* **740**, L20 (2011), arXiv:1108.0947 [astro-ph.CO].
- [32] T. Jacobson and R. Parentani, *Found. Phys.* **33**, 323 (2003), arXiv:gr-qc/0302099.
- [33] S. Furlanetto, S. Oh, and F. Briggs, *Phys. Rept.* **433**, 181 (2006), arXiv:astro-ph/0608032.
- [34] T.-C. Chang, U.-L. Pen, J. B. Peterson, and

- P. McDonald, *Phys. Rev. Lett.* **100**, 091303 (2008), arXiv:0709.3672 [astro-ph].
- [35] A. Liu and M. Tegmark, *Phys. Rev. D* **83**, 103006 (2011), arXiv:1103.0281 [astro-ph.CO].
- [36] A. Liu and M. Tegmark, *MNRAS* **419**, 3491 (2012), arXiv:1106.0007 [astro-ph.CO].
- [37] J. Shaw, K. Sigurdson, U.-L. Pen, A. Stebbins, and M. Sitwell, *Astrophys. J.* **781**, 57 (2014), arXiv:1302.0327 [astro-ph.CO].
- [38] J. Shaw, K. Sigurdson, M. Sitwell, A. Stebbins, and U.-L. Pen, *Phys. Rev. D* **91**, 083514 (2015), arXiv:1401.2095 [astro-ph.CO].
- [39] A. R. Parsons, J. C. Pober, J. E. Aguirre, C. L. Carilli, D. C. Jacobs, and D. F. Moore, *ApJ* **756**, 165 (2012), arXiv:1204.4749 [astro-ph.IM].
- [40] J. C. Pober, A. Liu, J. S. Dillon, J. E. Aguirre, J. D. Bowman, R. F. Bradley, C. L. Carilli, D. R. DeBoer, J. N. Hewitt, D. C. Jacobs, M. McQuinn, M. F. Morales, A. R. Parsons, M. Tegmark, and D. J. Werthimer, *ApJ* **782**, 66 (2014), arXiv:1310.7031 [astro-ph.CO].
- [41] H.-J. Seo and C. M. Hirata, *Mon. Not. Roy. Astron. Soc.* **456**, 3142 (2016), arXiv:1508.06503 [astro-ph.CO].
- [42] J. C. Pober, *MNRAS* **447**, 1705 (2015), arXiv:1411.2050 [astro-ph.CO].
- [43] P. Bull, P. G. Ferreira, P. Patel, and M. G. Santos, *ApJ* **803**, 21 (2015), arXiv:1405.1452 [astro-ph.CO].
- [44] N. Dalal, O. Doré, D. Huterer, and A. Shirokov, *Phys. Rev. D* **77**, 123514 (2008), arXiv:0710.4560.
- [45] A. Slosar, C. Hirata, U. Seljak, S. Ho, and N. Padmanabhan, *Journal of Cosmology and Astro-Particle Physics* **2008**, 031 (2008), arXiv:0805.3580 [astro-ph].
- [46] S. Matarrese and L. Verde, *ApJ* **677**, L77 (2008), arXiv:0801.4826.
- [47] L. Verde and S. Matarrese, *ApJ* **706**, L91 (2009), arXiv:0909.3224.
- [48] N. Afshordi and A. J. Tolley, *Phys. Rev. D* **78**, 123507 (2008), arXiv:0806.1046.
- [49] V. Desjacques and U. Seljak, *Advances in Astronomy* **2010**, 908640 (2010), arXiv:1006.4763 [astro-ph.CO].
- [50] A. Barreira, *JCAP* **12**, 031 (2020), arXiv:2009.06622 [astro-ph.CO].
- [51] A. Barreira, *JCAP* **11**, 013 (2022), arXiv:2205.05673 [astro-ph.CO].
- [52] E. Fondi, L. Verde, F. Villaescusa-Navarro, M. Baldi, W. R. Coulton, G. Jung, D. Karagiannis, M. Liguori, A. Ravenni, and B. D. Wandelt, *JCAP* **02**, 048 (2024), arXiv:2311.10088 [astro-ph.CO].
- [53] S. Camera, M. G. Santos, P. G. Ferreira, and L. Ferramacho, *Physical Review Letters* **111**, 171302 (2013), arXiv:1305.6928 [astro-ph.CO].
- [54] Y. Xu, X. Wang, and X. Chen, *Astrophys. J.* **798**, 40 (2015), arXiv:1410.7794 [astro-ph.CO].
- [55] J. Fonseca, S. Camera, M. Santos, and R. Maartens, *Astrophys. J. Lett.* **812**, L22 (2015), arXiv:1507.04605 [astro-ph.CO].
- [56] J. Fonseca, R. Maartens, and M. G. Santos, *MNRAS* **466**, 2780 (2017), arXiv:1611.01322.
- [57] M. Ballardini, W. L. Matthewson, and R. Maartens, *Mon. Not. Roy. Astron. Soc.* **489**, 1950 (2019), arXiv:1906.04730 [astro-ph.CO].
- [58] D. Karagiannis, J. Fonseca, R. Maartens, and S. Camera, *Phys. Dark Univ.* **32**, 100821 (2021), arXiv:2010.07034 [astro-ph.CO].
- [59] A. Slosar, Z. Ahmed, D. Alonso, M. A. Amin, E. J. Arena, K. Bandura, N. Battaglia, J. Blazek, P. Bull, E. Castorina, T.-C. Chang, L. Connor, R. Davé, C. Dvorkin, A. van Engelen, S. Ferraro, R. Flauger, S. Foreman, J. Frisch, D. Green, G. Holder, D. Jacobs, M. C. Johnson, J. S. Dillon, D. Karagiannis, A. A. Kurov, L. Knox, A. Liu, M. Loverde, Y.-Z. Ma, K. W. Masui, T. McClintock, K. Moodley, M. Munchmeyer, L. B. Newburgh, C. Ng, A. Nomerotski, P. O'Connor, A. Obuljen, H. Padmanabhan, D. Parkinson, J. X. Prochaska, S. Rajendran, D. Rapetti, B. Salwanchik, E. Schaan, N. Sehgal, J. R. Shaw, C. Sheehy, E. Sheldon, R. Shirley, E. Silverstein, T. Slatyer, A. Slosar, P. Stankus, A. Stebbins, P. T. Timbie, G. S. Tucker, W. Tyndall, F. Villaescusa Navarro, B. Wallisch, and M. White, in *BAAS*, Vol. 51 (2019) p. 53, arXiv:1907.12559 [astro-ph.IM].
- [60] A. Pourtsidou, (2016), arXiv:1612.05138 [astro-ph.CO].
- [61] D. Karagiannis, A. Slosar, and M. Liguori, *JCAP* **11**, 052 (2020), arXiv:1911.03964 [astro-ph.CO].
- [62] H.-M. Zhu, U.-L. Pen, Y. Yu, and X. Chen, *Phys. Rev. D* **98**, 043511 (2018), arXiv:1610.07062 [astro-ph.CO].
- [63] N. G. Karaçaylı and N. Padmanabhan, *Mon. Not. Roy. Astron. Soc.* **486**, 3864 (2019), arXiv:1904.01387 [astro-ph.CO].
- [64] C. Modi, M. White, A. Slosar, and E. Castorina, *JCAP* **11**, 023 (2019), arXiv:1907.02330 [astro-ph.CO].
- [65] T. L. Makinen, L. Lancaster, F. Villaescusa-Navarro, P. Melchior, S. Ho, L. Perreault-Levasseur, and D. N. Spergel, *JCAP* **04**, 081 (2021), arXiv:2010.15843 [astro-ph.CO].
- [66] S. Cunnington *et al.*, *Mon. Not. Roy. Astron. Soc.* **523**, 2453 (2023), arXiv:2302.07034 [astro-ph.CO].
- [67] E. Sefusatti, M. Crocce, S. Pueblas, and R. Scoccamarro, *Phys. Rev. D* **74**, 023522 (2006), astro-ph/0604505.
- [68] M. Biagetti, L. Castiblanco, J. Noreña, and E. Sefusatti, *JCAP* **09**, 009 (2022), arXiv:2111.05887 [astro-ph.CO].
- [69] A. Barreira, *JCAP* **03**, 008 (2019), arXiv:1901.01243 [astro-ph.CO].
- [70] J. Salvalaggio, L. Castiblanco, J. Noreña, E. Sefusatti, and P. Monaco, (2024), arXiv:2403.08634 [astro-ph.CO].
- [71] V. Yankelevich and C. Porciani, *Mon. Not. Roy. Astron. Soc.* **483**, 2078 (2019), arXiv:1807.07076 [astro-ph.CO].
- [72] H. Gil-Marín, J. Noreña, L. Verde, W. J. Percival, C. Wagner, M. Manera, and D. P. Schneider, *Mon. Not. Roy. Astron. Soc.* **451**, 539 (2015), arXiv:1407.5668 [astro-ph.CO].
- [73] A. Lazanu, T. Giannantonio, M. Schmittfull, and E. P. S. Shellard, *Phys. Rev. D* **95**, 083511 (2017), arXiv:1511.02022.
- [74] I. Hashimoto, Y. Rasera, and A. Taruya, *Phys. Rev. D* **96**, 043526 (2017), arXiv:1705.02574 [astro-ph.CO].
- [75] K. C. Chan and L. Blot, *Phys. Rev. D* **96**, 023528 (2017), arXiv:1610.06585.
- [76] A. Oddo, E. Sefusatti, C. Porciani, P. Monaco, and A. G. Sánchez, *JCAP* **03**, 056 (2020), arXiv:1908.01774 [astro-ph.CO].
- [77] Y. Akrami *et al.* (Planck), *Astron. Astrophys.* **641**, A9 (2020), arXiv:1905.05697 [astro-ph.CO].
- [78] D. Karagiannis, R. Maartens, and L. F. Randrianjanahary, *JCAP* **11**, 003 (2022), arXiv:2206.07747 [astro-ph.CO].

- [79] A. Blanchard *et al.* (Euclid), *Astron. Astrophys.* **642**, A191 (2020), arXiv:1910.09273 [astro-ph.CO].
- [80] A. Barreira, *JCAP* **01**, 033 (2022), arXiv:2107.06887 [astro-ph.CO].
- [81] P. McDonald, *Phys. Rev. D* **78**, 123519 (2008), arXiv:0806.1061.
- [82] T. Lazeyras, A. Barreira, F. Schmidt, and V. Desjacques, *JCAP* **01**, 023 (2023), arXiv:2209.07251 [astro-ph.CO].
- [83] O. Doré, J. Bock, M. Ashby, P. Capak, A. Cooray, R. de Putter, T. Eifler, N. Flagey, Y. Gong, S. Habib, K. Heitmann, C. Hirata, W.-S. Jeong, R. Katti, P. Korngut, E. Krause, D.-H. Lee, D. Masters, P. Mausekopf, G. Melnick, B. Mennesson, H. Nguyen, K. Öberg, A. Pullen, A. Raccanelli, R. Smith, Y.-S. Song, V. Tolls, S. Unwin, T. Venumadhav, M. Viero, M. Werner, and M. Zemcov, arXiv e-prints, arXiv:1412.4872 (2014), arXiv:1412.4872 [astro-ph.CO].
- [84] T. Flöss, M. Biagetti, and P. D. Meerburg, *Phys. Rev. D* **107**, 023528 (2023), arXiv:2206.10458 [astro-ph.CO].
- [85] J. Wang *et al.*, *Mon. Not. Roy. Astron. Soc.* **505**, 3698 (2021), arXiv:2011.13789 [astro-ph.CO].
- [86] S. Cunningham *et al.*, *Mon. Not. Roy. Astron. Soc.* **518**, 6262 (2022), arXiv:2206.01579 [astro-ph.CO].
- [87] S. Paul, M. G. Santos, Z. Chen, and L. Wolz, (2023), arXiv:2301.11943 [astro-ph.CO].
- [88] A. Lewis, A. Challinor, and A. Lasenby, *ApJ* **538**, 473 (2000), astro-ph/9911177.
- [89] F. Schmidt, *Phys. Rev. D* **93**, 063512 (2016), arXiv:1511.02231.
- [90] V. Desjacques, D. Jeong, and F. Schmidt, *Phys. Rep.* **733**, 1 (2018), arXiv:1611.09787 [astro-ph.CO].
- [91] E. Castorina and F. Villaescusa-Navarro, *MNRAS* **471**, 1788 (2017), arXiv:1609.05157 [astro-ph.CO].
- [92] J. C. Jackson, *MNRAS* **156**, 1P (1972), arXiv:0810.3908.
- [93] J. A. Peacock and S. J. Dodds, *MNRAS* **267**, 1020 (1994), astro-ph/9311057.
- [94] W. E. Ballinger, J. A. Peacock, and A. F. Heavens, *MNRAS* **282**, 877 (1996), astro-ph/9605017.
- [95] T. Baldauf, U. Seljak, and L. Senatore, *Journal of Cosmology and Astro-Particle Physics* **4**, 006 (2011), arXiv:1011.1513 [astro-ph.CO].
- [96] M. Tellarini, A. J. Ross, G. Tasinato, and D. Wands, *Journal of Cosmology and Astro-Particle Physics* **6**, 014 (2016), arXiv:1603.06814.
- [97] S. Camera, M. G. Santos, and R. Maartens, *Mon. Not. Roy. Astron. Soc.* **448**, 1035 (2015), [Erratum: *Mon. Not. Roy. Astron. Soc.* **467**, 1505–1506 (2017)], arXiv:1409.8286 [astro-ph.CO].
- [98] F. Bernardeau, S. Colombi, E. Gaztañaga, and R. Scoccimarro, *Phys. Rep.* **367**, 1 (2002), astro-ph/0112551.
- [99] P. McDonald and A. Roy, *Journal of Cosmology and Astro-Particle Physics* **8**, 020 (2009), arXiv:0902.0991 [astro-ph.CO].
- [100] T. Baldauf, U. Seljak, V. Desjacques, and P. McDonald, *Phys. Rev. D* **86**, 083540 (2012), arXiv:1201.4827 [astro-ph.CO].
- [101] T. Giannantonio and C. Porciani, *Phys. Rev. D* **81**, 063530 (2010), arXiv:0911.0017 [astro-ph.CO].
- [102] Planck Collaboration, N. Aghanim, Y. Akrami, M. Ashdown, J. Aumont, C. Baccigalupi, M. Ballardini, A. J. Banday, R. B. Barreiro, N. Bartolo, S. Basak, R. Battye, K. Benabed, J. P. Bernard, M. Bersanelli, P. Bielewicz, J. J. Bock, J. R. Bond, J. Borrill, F. R. Bouchet, F. Boulanger, M. Bucher, C. Burigana, R. C. Butler, E. Calabrese, J. F. Cardoso, J. Carron, A. Challinor, H. C. Chiang, J. Chluba, L. P. L. Colombo, C. Combet, D. Contreras, B. P. Crill, F. Cuttaia, P. de Bernardis, G. de Zotti, J. Delabrouille, J. M. Delouis, E. Di Valentino, J. M. Diego, O. Doré, M. Douspis, A. Ducout, X. Dupac, S. Dusini, G. Efstathiou, F. Elsner, T. A. Enßlin, H. K. Eriksen, Y. Fantaye, M. Farhang, J. Fergusson, R. Fernandez-Cobos, F. Finelli, F. Forastieri, M. Frailis, A. A. Fraisse, E. Franceschi, A. Frolov, S. Galeotta, S. Galli, K. Ganga, R. T. Génova-Santos, M. Gerbino, T. Ghosh, J. González-Nuevo, K. M. Górski, S. Gratton, A. Gruppuso, J. E. Gudmundsson, J. Hamann, W. Handley, F. K. Hansen, D. Herranz, S. B. Hildebrandt, E. Hivon, Z. Huang, A. H. Jaffe, W. C. Jones, A. Karacki, E. Keihänen, R. Keskitalo, K. Kiiveri, J. Kim, T. S. Kisner, L. Knox, N. Krachmalnicoff, M. Kunz, H. Kurki-Suonio, G. Lagache, J. M. Lamarre, A. Lasenby, M. Lattanzi, C. R. Lawrence, M. Le Jeune, P. Lemos, J. Lesgourgues, F. Levrier, A. Lewis, M. Liguori, P. B. Lilje, M. Lilley, V. Lindholm, M. López-Cañiego, P. M. Lubin, Y. Z. Ma, J. F. Macías-Pérez, G. Maggio, D. Maino, N. Mandolesi, A. Mangilli, A. Marcos-Caballero, M. Maris, P. G. Martin, M. Martinelli, E. Martínez-González, S. Matarrese, N. Mauri, J. D. McEwen, P. R. Meinhold, A. Melchiorri, A. Mennella, M. Migliaccio, M. Millea, S. Mitra, M. A. Miville-Deschênes, D. Molinari, L. Montier, G. Morgante, A. Moss, P. Natoli, H. U. Nørgaard-Nielsen, L. Pagano, D. Paoletti, B. Partridge, G. Patanchon, H. V. Peiris, F. Perrotta, V. Pettorino, F. Piacentini, L. Polastri, G. Polenta, J. L. Puget, J. P. Rachen, M. Reinecke, M. Remazeilles, A. Renzi, G. Rocha, C. Rosset, G. Roudier, J. A. Rubiño-Martín, B. Ruiz-Granados, L. Salvati, M. Sandri, M. Savelainen, D. Scott, E. P. S. Shellard, C. Sirignano, G. Sirri, L. D. Spencer, R. Sunyaev, A. S. Suur-Uski, J. A. Tauber, D. Tavagnacco, M. Tenti, L. Toffolatti, M. Tomasi, T. Trombetti, L. Valenziano, J. Valiviita, B. Van Tent, L. Vibert, P. Vielva, F. Villa, N. Vittorio, B. D. Wandelt, I. K. Wehus, M. White, S. D. M. White, A. Zacchei, and A. Zonca, *A&A* **641**, A6 (2020), arXiv:1807.06209 [astro-ph.CO].
- [103] C. Alcock and B. Paczynski, *Nature* **281**, 358 (1979).
- [104] H.-J. Seo and D. J. Eisenstein, *Astrophys. J.* **598**, 720 (2003), arXiv:astro-ph/0307460.
- [105] Y.-S. Song, A. Taruya, and A. Oka, *Journal of Cosmology and Astro-Particle Physics* **8**, 007 (2015), arXiv:1502.03099.

APPENDIX

The tree-level HI IM power spectrum and bispectrum model in redshift space for operational modes SD, IF are given by :

$$\begin{aligned}
P_{\text{HI}}^{\text{SD,IF}}(\mathbf{k}, z) &= W^{\text{SD,IF}}(\mathbf{k})^2 \left[T_b(z)^2 \left[D_{\text{FOG}}^P(\mathbf{k}, z) Z_1(\mathbf{k}, z)^2 P_m^L(k, z) + P_\varepsilon(z) \right] + P_{\text{N}}^{\text{SD,IF}}(\mathbf{k}, z) \right], \quad (7) \\
B_{\text{HI}}^{\text{SD,IF}}(\mathbf{k}_1, \mathbf{k}_2, \mathbf{k}_3, z) &= W^{\text{SD,IF}}(\mathbf{k}_1) W^{\text{SD,IF}}(\mathbf{k}_2) W^{\text{SD,IF}}(\mathbf{k}_3) T_b(z)^3 \\
&\times \left[D_{\text{FOG}}^B(\mathbf{k}_1, \mathbf{k}_2, \mathbf{k}_3, z) \left[Z_1(\mathbf{k}_1, z) Z_1(\mathbf{k}_2, z) Z_1(\mathbf{k}_3, z) B_p(k_1, k_2, k_3, z) \right. \right. \\
&+ \left. \left. \left\{ 2Z_1(\mathbf{k}_1, z) Z_1(\mathbf{k}_2, z) Z_2(\mathbf{k}_1, \mathbf{k}_2, z) P_m^L(k_1, z) P_m^L(k_2, z) + 2 \text{ perm} \right\} \right] \right. \\
&\left. + 2P_{\varepsilon\varepsilon\delta}(z) \left[Z_1(\mathbf{k}_1, z) P_m^L(k_1, z) + 2 \text{ perm} \right] + B_\varepsilon(z) \right]. \quad (8)
\end{aligned}$$

Here P_m^L is the linear matter power spectrum, as given by CAMB [88], while B_p is the primordial bispectrum for local PNG. The instrumental noise $P_{\text{N}}^{\text{SD,IF}}$ is different for each operational mode, with different scale behaviour, and depends on the HI IM survey specifications: see [43, 58] for details. The background temperature is given by $\bar{T} = 188 \Omega_{\text{HI}}(z) h(1+z)^2 H_0/H(z) \mu\text{K}$, while the HI density evolution is modelled as $\Omega_{\text{HI}}(z) = 4 \times 10^{-4} (1+z)^{0.6}$ [27]. The stochastic contributions are given by $P_\varepsilon(z) = 1/\bar{n}(z)$, $P_{\varepsilon\varepsilon\delta}(z) = b_1(z)/\bar{n}(z)$ and $B_\varepsilon(z) = 1/\bar{n}^2(z)$ [89, 90], where \bar{n} is the effective number density of HI IM [91]. These shot-noise terms can be neglected for HI IM, since they are small for the scales we consider [28, 43]. Thus, the instrumental noise is the dominant noise contribution for an HI IM. The effect of the velocity dispersion, the fingers-of-god effect (FoG), is described by a phenomenological by a damping factor [92–94] and given by $D_{\text{FOG}}^P(\mathbf{k}) = \exp[-(k\mu\sigma_P)^2]$ and $D_{\text{FOG}}^B(\mathbf{k}_1, \mathbf{k}_2, \mathbf{k}_3) = \exp[-(k_1^2\mu_1^2 + k_2^2\mu_2^2 + k_3^2\mu_3^2)\sigma_B^2]$ for the power spectrum and bispectrum respectively. The damping amplitudes σ_P and σ_B are given by the linear velocity dispersion σ_v .

The redshift kernels up to second order, which include local PNG, are [9, 95, 96]:

$$\begin{aligned}
Z_1(\mathbf{k}_i, z) &= b_1(z) + f(z)\mu_i^2 + \frac{f_{\text{NL}}^{\text{loc}} b_\phi(z)}{M(k_i, z)}, \quad (9) \\
Z_2(\mathbf{k}_i, \mathbf{k}_j, z) &= b_1(z)F_2(\mathbf{k}_i, \mathbf{k}_j) + f(z)\mu_{ij}^2 G_2(\mathbf{k}_i, \mathbf{k}_j) + \frac{b_2(z)}{2} + \frac{b_{s^2}(z)}{2} S_2(\mathbf{k}_i, \mathbf{k}_j) \\
&+ \frac{f(z)\mu_{ij}k_{ij}}{2} \left[\frac{\mu_i}{k_i} Z_1(\mathbf{k}_j, z) + \frac{\mu_j}{k_j} Z_1(\mathbf{k}_i, z) \right] \\
&+ f_{\text{NL}}^{\text{loc}} \left[\frac{b_{\phi\delta}(z) - b_\phi(z)N_2(\mathbf{k}_j, \mathbf{k}_i)}{2M(k_i, z)} + \frac{b_{\phi\delta}(z) - b_\phi(z)N_2(\mathbf{k}_i, \mathbf{k}_j)}{2M(k_j, z)} \right]. \quad (10)
\end{aligned}$$

where $f(z)$ is the linear growth rate, $\mu_i = \hat{\mathbf{k}}_i \cdot \hat{\mathbf{z}}$, with $\hat{\mathbf{z}}$ being the line-of-sight vector, $\mu_{ij} = (\mu_i k_i + \mu_j k_j)/k_{ij}$ and $k_{ij}^2 = (\mathbf{k}_i + \mathbf{k}_j)^2$. The function $M(k, z) = 2c^2 D(z) T(k) k^2 / (3\Omega_m H_0^2 g_{\text{dec}})$, contains the linear growth factor $D(z)$ and matter transfer function $T(k)$, and g_{dec} is the Bardeen potential growth factor at decoupling (ensuring that $f_{\text{NL}}^{\text{loc}}$ is in the CMB convention [97]). The kernels $F_2(\mathbf{k}_i, \mathbf{k}_j)$ and $G_2(\mathbf{k}_i, \mathbf{k}_j)$ are the second-order symmetric SPT kernels [98], while $S_2(\mathbf{k}_1, \mathbf{k}_2) = (\hat{\mathbf{k}}_1 \cdot \hat{\mathbf{k}}_2)^2 - 1/3$ is the tidal kernel [99, 100]. The kernel $N_2(\mathbf{k}_1, \mathbf{k}_2) = (\mathbf{k}_1 \cdot \mathbf{k}_2)k_1^2$ encodes the coupling of the PNG potential to the Eulerian-to-Lagrangian displacement field [95, 101]. The bias parameters b_1 and b_2 are the HI linear and quadratic bias parameters, b_{s^2} is the tidal bias coefficient, while b_ϕ and $b_{\phi\delta}$ are the local PNG bias parameters. The expressions for the bias parameters can be found in [78], while the PNG bias is considered a function of the linear bias, i.e. $b_\phi(b_1)$ and $b_{\phi\delta}(b_1)$, using the ‘universality relation’ [90].

The full set of parameters consists of 5 cosmological parameters, the primordial PNG amplitude and 11 further parameters in each redshift bin i :

$$\begin{aligned}
\boldsymbol{\theta}(z_i) &= \left\{ \Omega_b, \Omega_c, h, A_s, n_s, f_{\text{NL}}^{\text{loc}}; \right. \\
&\left. D_A(z_i), H(z_i), f(z_i), b_1(z_i), b_2(z_i), b_{s^2}(z_i), \sigma_P(z_i), \sigma_B(z_i), P_\varepsilon(z_i), P_{\varepsilon\varepsilon\delta}(z_i), B_\varepsilon(z_i) \right\}. \quad (11)
\end{aligned}$$

For the 5 cosmological parameters we add prior information from the observation of CMB performed by Planck [102]. We assume redshift bins are independent, so that e.g. $\partial P(\mathbf{k}, z_i)/\partial \theta_\alpha(z_j) = 0$ for $i \neq j$. All the above parameters are considered unknown and are marginalized over in the Fisher matrix formalism. Note that we also consider the anisotropies induced in the observed galaxy clustering by the Alcock-Paczynski effect [103], which occurs when the fiducial cosmology, used to convert the observed angular coordinates and redshifts to physical distances, differs from the true one [104, 105].

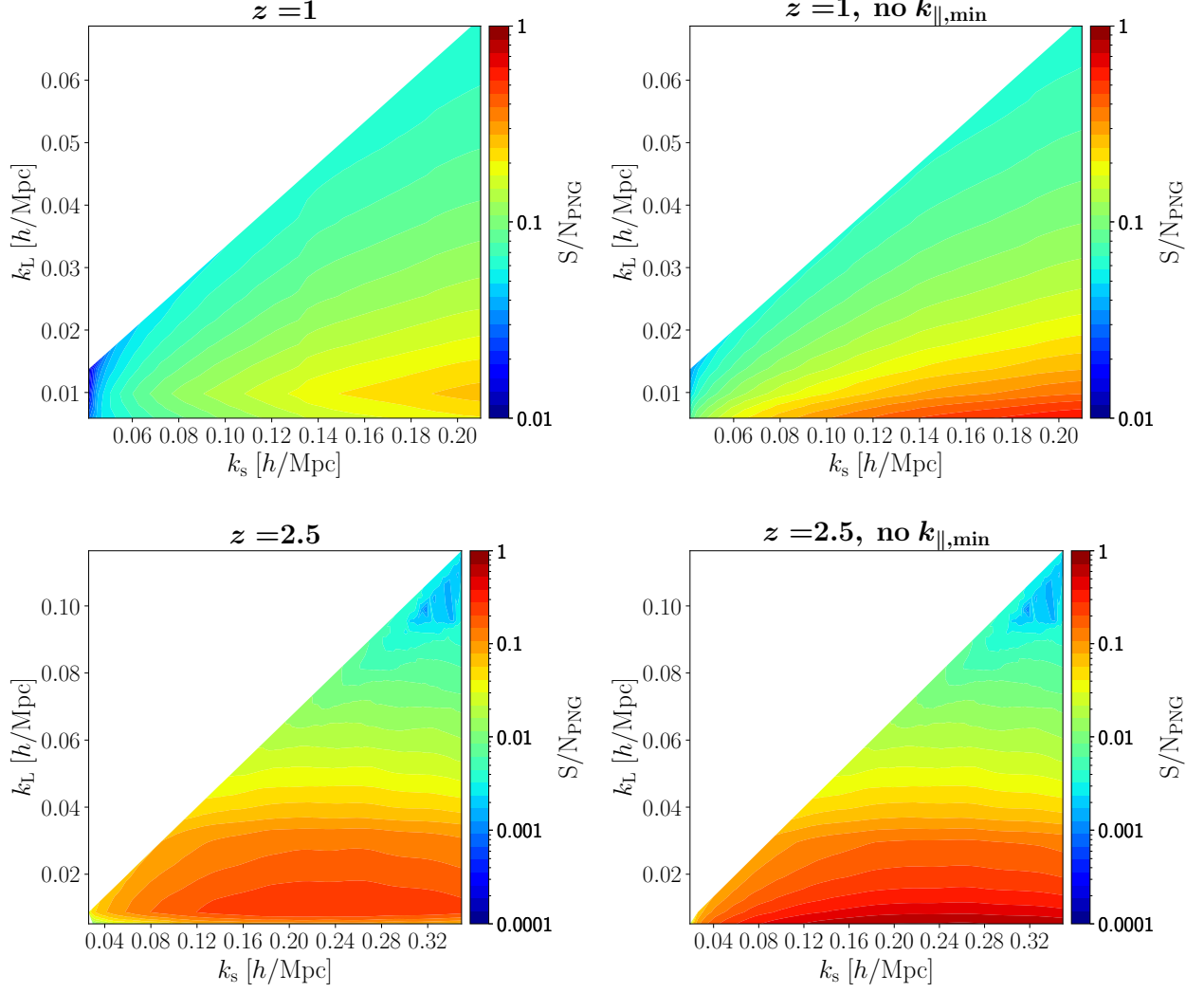


FIG. 3: Normalized non-Gaussian SNR [Eq. (12)] as a function of the long- and short-wavelength modes of the squeezed configuration (i.e. $k_1 = k_2 = k_S$ and $k_3 = k_L$), after integrating over the triangle orientation with the line-of-sight. Upper panels are at redshift $z = 1$, lower at $z = 2.5$. The left column is the fiducial case, while the right is the case where no radial foregrounds are considered (i.e. no $k_{\parallel, \min}$ cut).

To investigate the effect of the radial foreground cut, we calculate the PNG signal-to-noise ratio (SNR), as a function of the sides of the squeezed triangles, i.e. the long-wavelength ($k_3 = k_L$) and short-wavelength ($k_1 = k_2 = k_S$) modes. The signal-to-noise ratio of the HI IM bimodal bispectrum is given by

$$(S/N)_{\text{PNG}}^2(z) = \int d^3 \mathbf{k} B_{\text{PNG}}^{\text{SD} \times \text{IF}}(\mathbf{k}_i, z) (\mathbf{C}^{\text{G}})_{ij}^{-1} B_{\text{PNG}}^{\text{SD} \times \text{IF}}(\mathbf{k}_j, z), \quad (12)$$

where $B_{\text{PNG}} = B(f_{\text{NL}}^{\text{loc}} \neq 0) - B(f_{\text{NL}}^{\text{loc}} = 0)$. After integrating over the angles that define the orientation of the triangle with the line of sight, the SNR results are shown in Fig. 3, at redshifts $z = 1$ and $z = 2.5$. The results are presented for two cases: k -modes affected by the radial foregrounds are excluded from the analysis, i.e. $k_{\parallel} < k_{\parallel, \min}$ (left column of panels in Fig. 3); k -modes affected by the radial foregrounds are fully recovered and utilised in the S/N (right

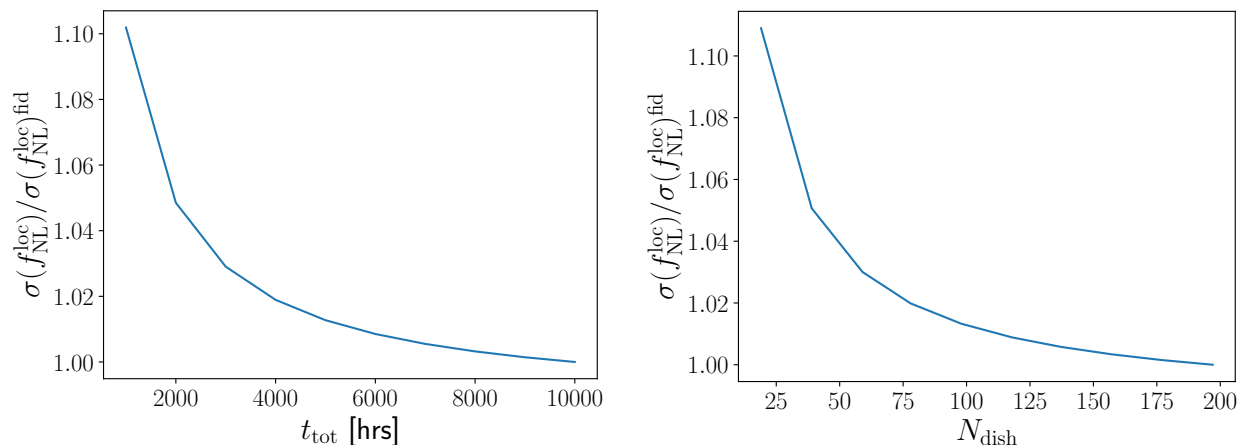


FIG. 4: Marginalized 1σ forecasts on $f_{\text{NL}}^{\text{loc}}$, normalized to the fiducial constraints (i.e. SKA \times HIRAX in Fig. 2) as a function of the time of the single-dish survey t_{tot} (left panel) and the number of dishes N_{dish} (right panel).

column of panels in Fig. 3).

For the low redshift bin ($z = 1$), the bulk of the local PNG signal is located in bispectrum modes that are beyond the linear regime, i.e. $k_1 \sim k_2 = k_S > k_{\text{max}}$. In the case where the long-wavelength radial modes are lost to the foregrounds, only a small part of the maximal PNG S/N is accessed. However, if the radial foregrounds are cleaned and the lost k -modes fully reconstructed, more squeezed triangles, carrying maximal PNG signal, are now within the perturbative regime and within the reach of linear theory. Accessing the rest of the signal necessitates k_S to be in the nonlinear regime and beyond the validity of the tree-level analytic model. This would allow the formation of more squeezed triangles, while significantly boosting the contribution of these low redshifts to the total local PNG signal.

On the other hand the high redshift bin ($z = 2.5$), which corresponds to a time where the Universe was less nonlinear, allows for most of the PNG S/N to be well within the perturbative regime. These higher redshifts seem to provide the main contribution to the total PNG bispectrum constraints, as shown in the lower row of panels in Fig. 3. Even in the presence of a radial foreground cut, most of the PNG S/N is still within the reach of the tree-level analytic model. Utilising these scales in the analysis increases the number of squeezed triangles, especially those with a maximal PNG signal, boosting the constraints on $f_{\text{NL}}^{\text{loc}}$. Pushing towards smaller scales, i.e. $k_S > k_{\text{max}}$, would provide access to more configurations, although it is not necessary for these redshift bins to provide a significant contribution to the total $f_{\text{NL}}^{\text{loc}}$ constraints. This explains why we observe a greater improvement in the final $f_{\text{NL}}^{\text{loc}}$ forecasts, as shown in Fig. 2, if we include the long-wavelength radial k -modes lost to foregrounds in the analysis, rather than pushing towards smaller scales by increasing the value of k_{max} . Although this shows the importance of accessing the very large scales with HI IM, it provides an alternative to compensate the signal lost to the 21cm foregrounds by venturing towards the nonlinear regime.

At low redshifts, the bulk of the signal arises from squeezed triangles that satisfy $k_3 = k_L \lesssim 0.02 h/\text{Mpc}$, while at high redshifts, it is from triangles that satisfy $k_3 = k_L \lesssim 0.05 h/\text{Mpc}$. This indicates that accessing enough long-wavelength k -modes with the SD mode survey is important for the proposed method to provide competitive constraints, independently of whether or not the radial foregrounds are cleaned. Thus, to investigate this further, we produce $f_{\text{NL}}^{\text{loc}}$ forecasts by following the recipe described in the main text, while varying one of the parameters that control the capability of the SD survey (i.e. SKA) to adequately probe the large scales. These are the integration time (t_{tot}) and the number of dishes (N_{dish}). Increasing any of the parameters reduces the instrumental noise and therefore the uncertainty on $f_{\text{NL}}^{\text{loc}}$.

The forecast $\sigma(f_{\text{NL}}^{\text{loc}})$, normalized to the fiducial SD survey specifications used to derive the main results (Fig. 2), is shown in Fig. 4 as a function of t_{tot} (left panel) and N_{dish} (right panel). Decreasing by an order of magnitude the capabilities of the SD mode survey (e.g. considering only 20 dishes out of 200 or 1000 hrs instead of 10000 hrs), degrades the $f_{\text{NL}}^{\text{loc}}$ constraint by only $\sim 10\%$. This indicates that the effect of the instrumental noise of the SD mode survey is small, since it is still able to efficiently probe the large scales. We use as an example a variation of the SD survey, ‘SKA/2’, where the integrated time t_{tot} and the number of dishes N_{dish} are reduced by half. The bimodal bispectrum $f_{\text{NL}}^{\text{loc}}$ forecasts are presented in Fig. 5 (SKA/2 \times HIRAX) by following the process described in the main text. Moreover, the idealized case where the radial k -modes lost to foregrounds are reconstructed (i.e. no $k_{\parallel\text{min}}$ cut), is also shown in dashed lines. The results show that reducing the capabilities of the SD survey by half, has minimal

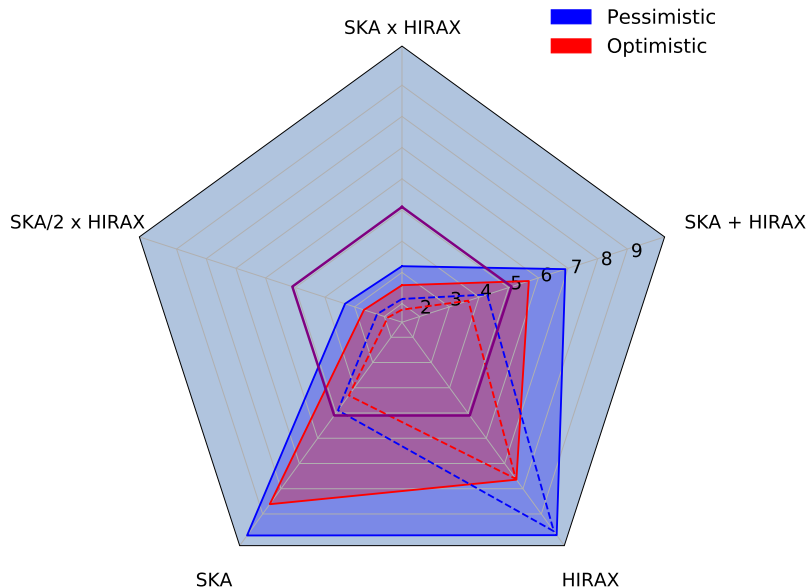


FIG. 5: Marginalized 1σ forecasts on $f_{\text{NL}}^{\text{loc}}$ from the bimodal bispectrum (SKA \times HIRAX), in the case of the pessimistic and optimistic k_{max} . A bimodal case with the capability of the SD survey (SKA) significantly diminished (the number of dishes and observational time are reduced to half), is also presented (SKA/2 \times HIRAX). Forecasts from each individual survey, as well as their summed signal (SKA + HIRAX) are presented for comparison. Planck 2018 constraints [77] are indicated with a purple line. The dashed line correspond to the idealised case, where the radial signal lost to foregrounds is recovered (i.e. no $k_{\parallel\text{min}}$ cut is applied). This represents the maximal constraints from the proposed bimodal method.

effect on the bimodal constraints on $f_{\text{NL}}^{\text{loc}}$. This is true for both values of k_{max} (‘Pessimistic’ and ‘Optimistic’) and for the cases where the modes $k_{\parallel} < k_{\parallel\text{min}}$ are included (dashed lines) and excluded (solid lines) from the analysis. The tightest constraint, $\sigma(f_{\text{NL}}^{\text{loc}}) \sim 2$, corresponds to the optimistic k_{max} and the case with no $k_{\parallel\text{min}}$ cut.

The advantages of the bimodal bispectrum are not limited to squeezed configurations and other shapes can be utilised. In Fig. 6 we show forecasts on $f_{\text{NL}}^{\text{loc}}$ when all triangle configurations are used and a redshift independent $k_{\text{max}} = 0.2 h/\text{Mpc}$ is considered. Note that the complete bimodal bispectrum covariance is used in these forecasts, since the approximate expression for the non-Gaussian part [Eq. (5)] is accurate, for the scales considered, in the case of all shapes of triangles [84]. The bimodal bispectrum still provides a significant improvement over the constraints from each individual survey (a factor of ~ 2), while it exhibits a $\sim 30\%$ improvement over their summed signal. Pushing k_{max} to smaller values would enhance these differences even further, as shown in the main text.

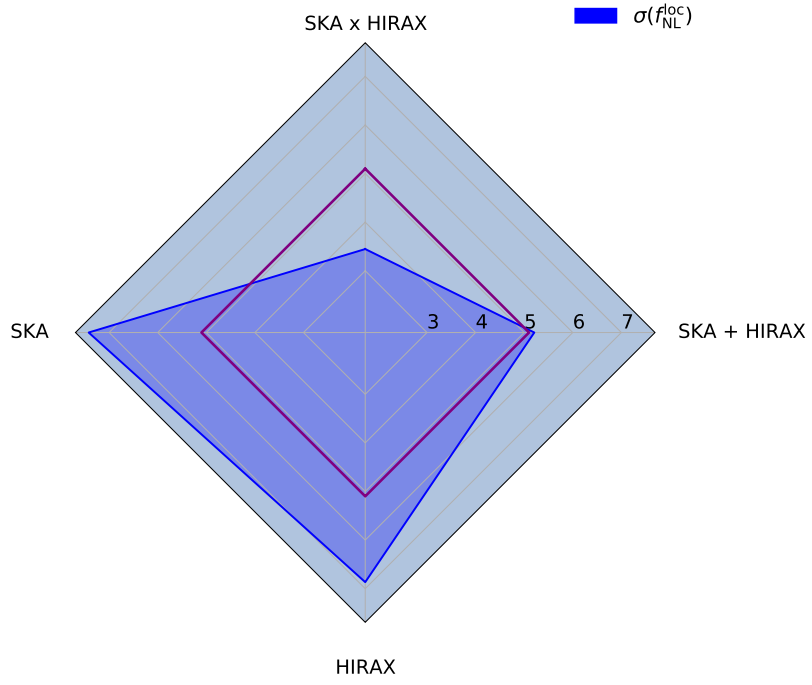


FIG. 6: Same as Fig. 2, but for all triangle shapes, not only squeezed, and with a fixed $k_{\max}(z) = 0.2 h/\text{Mpc}$.